Applied Catalysis B: Environmental 288 (2021) 119993

Contents lists available at ScienceDirect

Applied Catalysis B: Environmental

journal homepage: www.elsevier.com/locate/apcatb

Carbon nitride nanotubes with in situ grafted hydroxyl groups for highly efficient spontaneous H_2O_2 production

Liang Zhou [a,d], Juying Lei [a,b,d,*], Fuchen Wang [e], Lingzhi Wang [c,d], Michael R. Hoffmann [f], Yongdi Liu [a,b,d], Su-Il In [f,g,**], Jinlong Zhang [c,d,***]

[a] State Environmental Protection Key Laboratory of Environmental Risk Assessment and Control on Chemical Process, East China University of Science and Technology, 130 Meilong Road, Shanghai 200237, PR China
[b] Shanghai Institute of Pollution Control and Ecological Security, Shanghai 200092, PR China
[c] Key Laboratory for Advanced Materials and Joint International Research Laboratory of Precision Chemistry and Molecular Engineering, Feringa Nobel Prize Scientist Joint Research Center, School of Chemistry and Molecular Engineering, East China University of Science and Technology, 130 Meilong Road, Shanghai 200237, PR China
[d] Shanghai Engineering Research Center for Multi-media Environmental Catalysis and Resource Utilization, East China University of Science and Technology, 130 Meilong Road, Shanghai 200237, PR China
[e] Institute of Clean Coal Technology, East China University of Science and Technology, Shanghai 200237, PR China
[f] Department of Environmental Science & Engineering, Linde + Robinson Laboratories, California Institute of Technology, Pasadena, CA, 91125, USA
[g] Department of Energy Science & Engineering, DGIST, 333 Techno Jungang-daero, Hyeonpung-eup, Dalseong-gun, Daegu 42988, Republic of Korea

ARTICLE INFO

Keywords:
g-C_3N_4
Hydroxyl groups
Photocatalysis
Spontaneous
H_2O_2 production

ABSTRACT

An active and inexpensive photocatalyst for H_2O_2 production is desirable for industrial applications. However, obtaining high photocatalytic activity from metal-free catalysts without the use of sacrificial electron donors is difficult. Herein, g-C_3N_4 (CN) nanotubes functionalized with surface > OH groups that are grafted in situ were successfully synthesized via a novel alkalinization process. The nanotube structures provide a large surface area and improved mass transfer properties. In situ grafted > OH groups can capture photogenerated holes to promote separation of photogenerated charge, enabling the ready availability of electrons and hydrogen ions for H_2O_2 production. Further, the surface > OH groups help to suppress H_2O_2 self-decomposition. Consequently, a high rate of 240.36 μmol h^{-1} g^{-1} of H_2O_2 production can be achieved without sacrificial agents, which is the highest H_2O_2 production in a spontaneous system for metal-free photocatalysts. This work provides a new strategy for an efficient and spontaneous H_2O_2 production method using a metal-free CN photocatalyst.

1. Introduction

Hydrogen Peroxide (H_2O_2) is widely used in biological processes, environmental remediation, and more broadly in the chemical industry [1,2]. However, reagent and commercial grade H_2O_2 is mainly produced via the anthraquinone method, alcohol oxidation, or electrochemical synthesis [3–6]. Unfortunately, these synthetic methods require a significant amount of energy. Furthermore, the resulting organic by-products are generally harmful to the environment [7,8]. Therefore, developing an economical, efficient, and environmentally friendly method for H_2O_2 production is desirable.

Semiconductor photocatalytic reduction of O_2 in H_2O to produce H_2O_2 provides an alternative and viable approach [9–13]. For example, Teranishi et al. utilized a hybrid photocatalyst, Au/TiO_2, for H_2O_2 production [14], while Kim et al. used a graphene oxide/CdS hybrid composite to produce H_2O_2 by harnessing low-energy photons (635 nm) [15]. Shiraishi et al. found that mesoporous g-C_3N_4 (CN) with surface defects was a better photocatalyst than bulk phase CN for steady-state

* Corresponding author at: State Environmental Protection Key Laboratory of Environmental Risk Assessment and Control on Chemical Process, East China University of Science and Technology, 130 Meilong Road, Shanghai 200237, PR China.
** Corresponding author at: Department of Environmental Science & Engineering, Linde + Robinson Laboratories, California Institute of Technology, Pasadena, CA, 91125, USA.
*** Corresponding author at: Key Laboratory for Advanced Materials and Joint International Research Laboratory of Precision Chemistry and Molecular Engineering, Feringa Nobel Prize Scientist Joint Research Center, School of Chemistry and Molecular Engineering, East China University of Science and Technology, 130 Meilong Road, Shanghai 200237, PR China.
E-mail address: leijuying@ecust.edu.cn (J. Lei).

https://doi.org/10.1016/j.apcatb.2021.119993
Received 23 December 2020; Received in revised form 6 February 2021; Accepted 6 February 2021
Available online 14 February 2021

H_2O_2 production [16]. Sacrificial reagents are often employed during semiconductor photocatalytic H_2O_2 production in order to reduce either its subsequent oxidation or reduction leading to a steady-state limiting production rate. Ethanol (EtOH) is often used as a sacrificial agent; photogenerated holes oxidize EtOH and produce hydrogen ions and ethyl aldehyde as written in Eq. (1) allowing for the reduction of oxygen to H_2O_2 in Eq. (2) [17]. However, the continuous addition of a costly sacrificial agent does not provide a sustainable solution.

$$RCH_2OH + 2h^+ \rightarrow RCHO + 2H^+ \quad (1)$$

$$O_2 + 2H^+ + 2e^- \rightarrow H_2O_2 \quad (2)$$

Kofuji et al. reported on a carbon nitride-aromatic diimide-graphene nanohybrid for the photocatalytic production of H_2O_2 from water and O_2 without a sacrificial reagent under visible light illumination [18]. Hirakawa et al. reported on the use gold nanoparticles supported on $BiVO_4$ to achieve a two-electron reduction of O_2 resulting in improved H_2O_2 production rates [19]. Moon et al. employed a multi-component hybrid, CoPi-rGO/TiO_2, to produce H_2O_2 in the absence of added organic electron donors [20]. Improved photocatalytic production of H_2O_2 on semiconductor composites has been achieved by adjusting the bandgaps or by improving the light harvesting of the hybrid catalysts.

A major obstacle for the large-scale photocatalytic production of H_2O_2 with or without sacrificial reagents is the reduction of H_2O_2 by conduction-band electrons or the oxidation of H_2O_2 to hydroperoxyl radical and oxygen as shown in Eqs. (3)–(6) [15,21]. The photocatalytic production of H_2O_2 eventually reaches a steady-state maximum level due to the competition between reductive formation and subsequent oxidative loss pathways [21–24]. However, to the best of our knowledge, few studies have been focused on enhancing H_2O_2 production by suppressing the various decomposition reactions.

$$H_2O_2 + H^+ + e^- \rightarrow H_2O + OH^\bullet \quad (3)$$

$$H_2O_2 + 2H^+ + 2e^- \rightarrow 2H_2O \quad (4)$$

$$H_2O_2 + h^+ \rightarrow H^+ + HO_2^\bullet \quad (5)$$

$$H_2O_2 + 2h^+ \rightarrow O_2 + 2H^+ \quad (6)$$

Herein, we show synthesis via a novel preparation method and subsequent applications of alkalinized carbon nitride nanotubes (ACNT) as a catalytic platform. ACNTs have a stable structure with surface > OH groups grafted onto the nanotubes. The surface hydroxyl groups play an important role in enhancing H_2O_2 production. After hydroxylation, the photocatalytic production of H_2O_2 was enhanced by a factor of 13 using ACNTs compared to pristine CNs. In this report, we propose mechanism for increased H_2O_2 and a function of alkalinization and morphological modifications and for the inhibition of the self-decomposition of H_2O_2.

2. Experimental section

2.1. Preparation of g-C_3N_4

A porcelain crucible was loaded with melamine (10 g) and calcined at 550 °C for 4 h in air at a heating rate of 2.5 °C/min. The yellow sample was ground to a homogeneous power. The products were denoted as CN.

2.2. Preparation of g-C_3N_4 nanotubes

In a typical synthesis procedure, 1.0 g of melamine was added to 70 mL of distilled water and stirred at 80 °C. The solution was sealed in a poly(tetrafluoroethylene) (Teflon)-lined autoclave (100 mL) and heated at 200 °C for 10 h until it became clear and transparent. After completion of the solvothermal process, the formed solids were washed several times with EtOH to obtain melamine nanorods. A porcelain crucible was loaded with the nanorods and calcined at 550 °C for 4 h in air at a heating rate of 2.5 °C/min. The samples were washed, dried, and labeled as CNT.

2.3. Preparation of alkalinized carbon nitride nanotubes

Alkalinization and the solvothermal process were carried out simultaneously. Then, 1.0 g of melamine, 1.0, 5.0, or 10.0 g of KCl, and 0.2 g NH_4Cl were added to 70 mL of distilled water and stirred at 80 °C. The next steps performed were identical to those described to produce CNT. Samples with 1.0, 5.0, and 10.0 g KCl were labeled ACNT-1, ACNT-5, and ACNT-10, respectively.

2.4. Photocatalytic tests

Photocatalytic H_2O_2 production experiments were conducted with H_2O, EtOH, O_2, and simulated sunlight irradiation at ambient temperature (25 °C). Exactly 0.05 g of catalyst was suspended in 50 mL of distilled water in a quartz tube (For the control photocatalytic experiment in Fig. 8, 50 mL of distilled water was replaced by the mixture of 40 mL H_2O and 10 mL EtOH for photocatalytic H_2O_2 production, in which EtOH worked as a sacrificial agent). O_2 was then bubbled into this system for 20 min to obtain an O_2-equilibrated environment. Adsorption equilibrium was achieved following 30 min of stirring in the dark. Thereafter, the system was irradiated by simulated sunlight (AM1.5 filter) for 30 min. One milliliter of suspension was taken from reaction mixture and mixed with 2 mL of 0.1 M KI solution and 0.05 mL of 0.01 M ammonium molybdate solution for 5 min. Absorbance was detected by UV–vis diffuse reflectance spectroscopy. The concentration of H_2O_2 was calculated by using Eq. (7) [24], in which A stands for the absorbance value in 350 nm.

$$[H_2O_2]\ (\mu M) = (A - 0.00141)/0.05,\ 0 < A < 1 \quad (7)$$

3. Results and discussion

3.1. Synthetic mechanism and surface morphology

A post-alkalinization method was initially tried in order to prepare ACNTs, as shown in the upper part of Scheme 1. As part of path, bulk commercial melamine (Fig. 1A) was partially hydrolyzed by cyanuric acid during hydrothermal treatment with pure water. Nanorods were formed through the self-assembly of melamine with cyanuric acid (Fig. 1B) [25,26]. The CNTs were obtained after calcination in air (Fig. 1C). Conventional alkalinization was carried out [27,28]. These CNTs were dispersed in NaOH or KOH solution and then steamed slowly under continuous stirring in an oil bath at 120 °C. At this point, however, the nanotube structure of the CNTs was completely destroyed, and only fragmented and alkalinized CN was observed by TEM (Figs. 1D and S1). In another experiment, we synthesized the CNTs and then applied a mild mixed solution of KCl and NH_4Cl in the same post-treatment procedure; a partially destroyed nanotube structure (Fig. 1E) and inadequate degree of alkalinization were the result. We were able to optimize the experimental procedure by alkalinizing the precursor prior to nanotube formation as shown in the lower part of Scheme 1. First, the alkalinized melamine nanorods (Fig. 1F) were hydrothermally synthesized with KCl and NH_4Cl to produce CNTs. The nanotube structure was successfully maintained after thermal condensation polymerization (i.e. ACNT-1, ACNT-5 and ACNT-10).

Fig. 2A and B show the nanotube structure of the ACNTs. The length of tubes can exceed 20 microns with corresponding diameters between 1 and 3 μm. The hollow interior structures of the product ACNTs are confirmed in Fig. 2C. The TEM image of ACNT-5 provides a clear view of the nanotube wall and edge; the thin walls are displayed in Fig. 2D. The electron micrographs show that the transparent nanotubes with large internal volumes, which are beneficial for enhancing mass transfer in

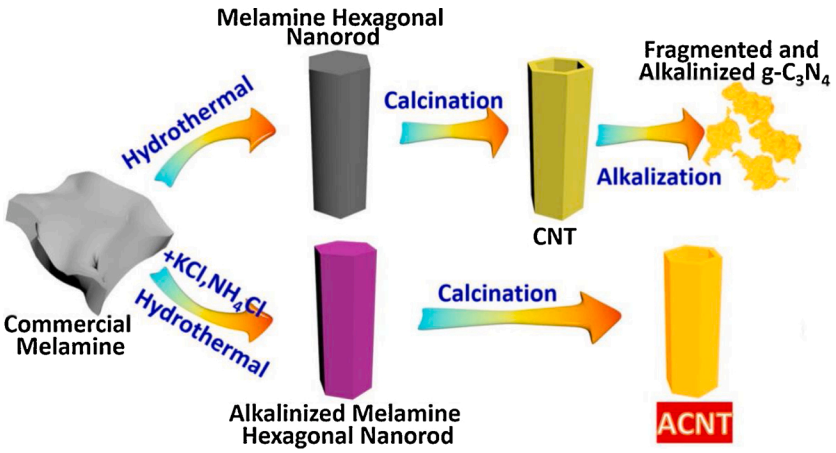

Scheme 1. Schematic of ACNT fabrication.

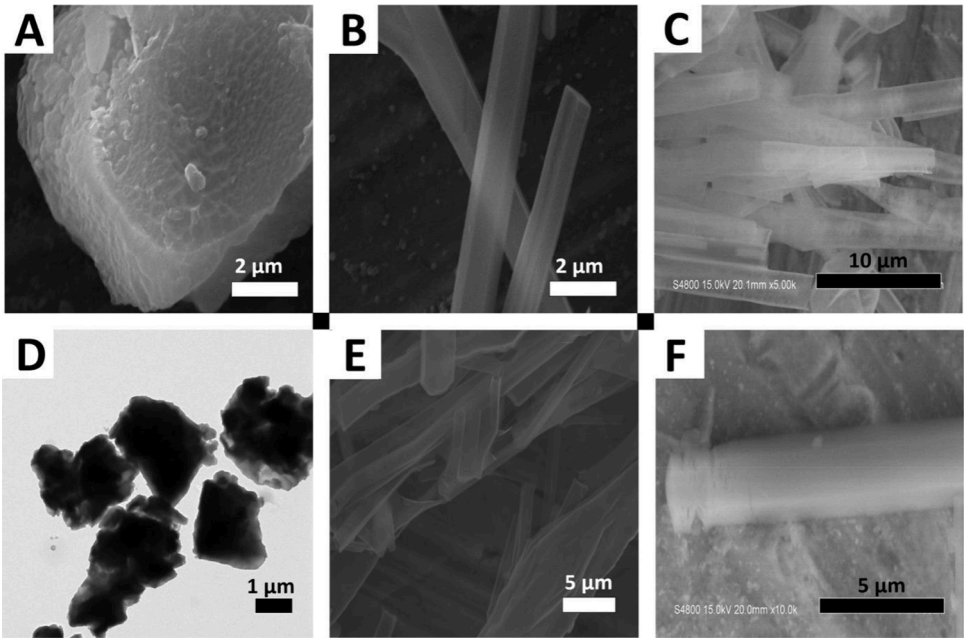

Fig. 1. (A) SEM image of commercial melamine. (B) SEM image of melamine nanorods. (C) FESEM image of CNTs. (D) TEM image of fragmented and alkalinized CN treated with KOH. (E) SEM image of alkalinized CN treated with NH_4Cl and KCl. (F) FESEM image of alkalinized melamine nanorods.

liquid-phase reactions. The morphologies of CN, ACNT-1, and ACNT-10 (Fig. S2) were explored for comparison with that of ACNT-5 (Fig. 2). CN has a layered structure with an inhomogeneous surface. Despite showing different degrees of alkalinity, ACNT-1 and ACNT-10 reveal uniform and complete nanotube structures. Therefore, the proposed experimental procedure effectively prevents the destruction of nanorod structure. The BET surface area (Fig. S3) of ACNT-5 was determined to be 63.53 m^2 g^{-1}, which is larger than that of the CNs (8.13 m^2 g^{-1}). Thus, the nanotube structure provides a sufficiently large surface area for access to reactive surface sites and to provide for improved mass transfer [29].

3.2. Physical and chemical properties

Several technologies were employed to understand the chemical structure of the catalysts. The XRD patterns in Fig. S4 reveal that all the samples have a distinct diffraction peak at approximately 27−28°, which correspond to the (002) planes of CN [30–32]. The crystal phase observed during alkalinization is identical to that of pristine CN. A shift toward larger angles and a significant decrease in intensity can be observed in samples with a nanotube structure. This result indicates a decrease in the layer distances of the (002) planes that are caused by the modifications due to alkalinization [33,34].

FTIR spectra of the samples (Fig. 3A) show the bands of triazine units and aromatic CN heterocycles at 808 and 1200–1680 cm^{-1}, respectively. In comparison to the CN spectra, two additional peaks are found in the ACNT-5 spectra. The two bands located at 999 and 2140 cm^{-1} are attributed to >OH groups on the surface of CN. The use of K^+ (i.e., KOH) during alkalinization is most likely responsible for hydroxylation of the CN surface. The band at 2177 cm^{-1} in the ACNT-5 FTIR spectrum is ascribed to a carbon nitrogen a moiety such as —C≡N [35–38]. The same phenomena are also observed in the spectra of ACNT-1, ACNT-10, and alkalinized CN, which were treated with KOH (Fig. S5).

High-resolution N-1 s, O-1 s, and K-2p XPS spectra are shown in Fig. 3B–D. The deconvoluted N-1 s spectrum of CN shows the presence of three different N chemical bonds at 398.67, 399.78, and 401.01 eV. They can be attributed to s-triazine rings (C—N—C), N—C_3) and amino groups (C—N—H). The peak attributed to C—N—H groups shifts toward a lower binding energy (400.71 eV) in ACNT-5 in comparison with those

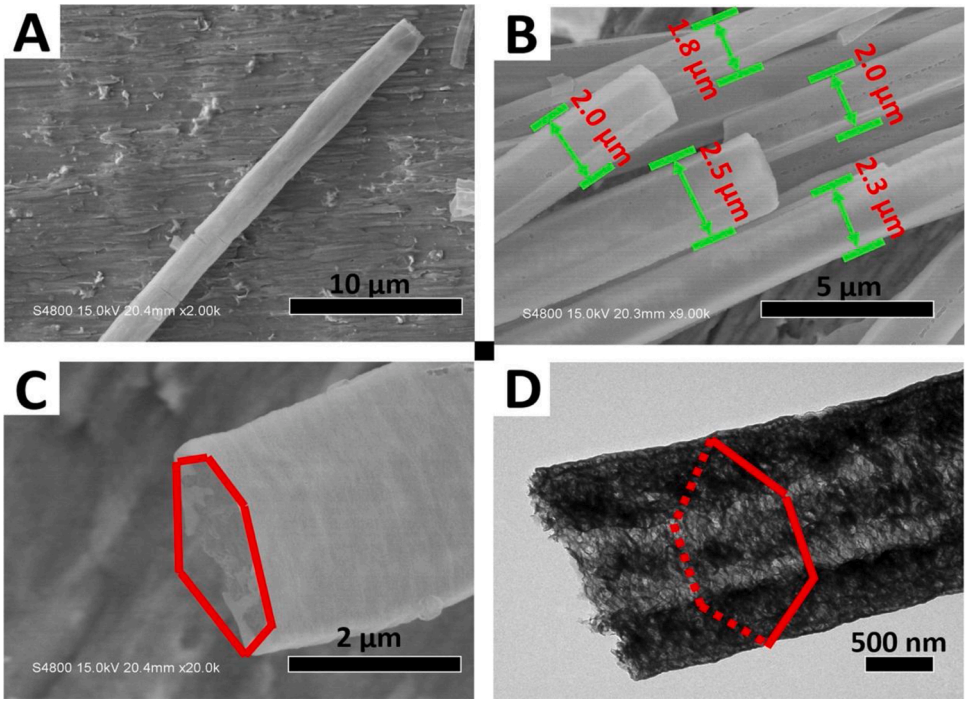

Fig. 2. (A–C) FESEM and (D) TEM images of ACNT-5.

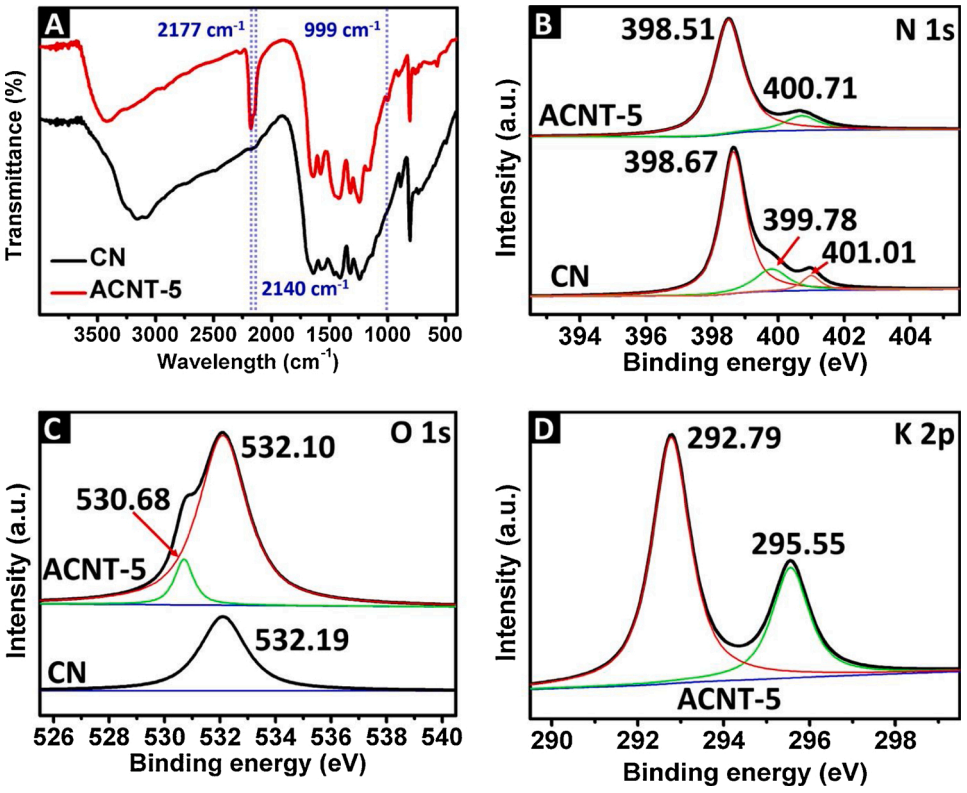

Fig. 3. (A) FTIR spectra of CN and ACNT-5, (B) N 1s, (C) O 1s, and (D) K 2p XPS spectra of CN and ACNT-5.

in other samples. This change can be explained by reductions in C—N—H and increases in C—O—H after alkalinization; moreover, N is more electronegative than C. Breakage of the bond between C and N may also partly explain this phenomenon. For example, introduction of K^+ could disrupt π-electron delocalization in the conjugated system and cause the N–C_3 bond to move toward a higher binding energy. A single peak at 532.19 eV is observed. This peak corresponds to bound water in the O 1s XPS spectrum of CN, while an additional peak at 530.68 eV is detected in the spectrum of ACNT-5; this new peak is attributed to O—H bonds. These observations are consistent with the FTIR and confirm that OH groups are successfully grafted onto CN. All of the bonds in the C 1s and N 1s spectra of ACNT shift toward lower binding energies compared

with those of CN, which indicates a strong interaction between K and N [35]. The peak observed at 292.79 eV suggests that K^+ is inserted into the inner planes of CN by mutual attraction to form the N—K bond in KN_3 [27,39]. The peak at 295.55 eV corresponds to the C—K bond. These bonds affect the surface electronic states of CN due to the electron withdrawing effect of K^+. It mainly reflects the increase in surface oxygen species and hydroxyl oxygen in the OH bands, which could be confirmed by the O 1s spectra [40]. This finding implies that introduction of K breaks the bond between C and N, which could be ascribed to the reaction between positively charged K^+ and the bonding electrons of C and N. OH groups dissociated from H_2O at high temperature form bonds with unsaturated C, and some new units (e.g., C≡N, $(N)_2C$—OH) are generated.

The different dispersibilities of the catalysts were studied. As shown in Fig. S6, ACNT-5 has considerably better dispersibility than CN under different treatments. The contact angles of the catalysts were determined, and all ACNT catalysts reveal contact angles smaller than that of CN (Fig. 4). This improvement in hydrophilicity further demonstrates the successful grafting of OH groups on the CN surface [41].

3.3. Photocatalytic H_2O_2 production in a spontaneous system

The photocatalytic activities of the ACNTs were evaluated by measuring the photocatalytic production of H_2O_2 under simulated sunlight in a spontaneous system as shown in Fig. 5A. Comparison of the CN and CNT results shows that production of H_2O_2 by the latter is approximately 2.3 times that by the former. Therefore, the nanotube structure most likely improves the photocatalytic activity by providing additional polar surface reaction sites and by improved mass transfer to the reaction sites. In addition to the nanotube structure, CN alkalinization further increases H_2O_2 production. For example, the alkalinized catalysts show production rates higher than those of CN and CNT. Indeed, 120.18 μM H_2O_2 is produced by ACNT-5 within 30 min; this quantity is higher than that reported by recent studies on spontaneous systems (Table S1). Moreover, the prolonged photoirradiation was used to evaluate the stability of photo-generated H_2O_2 (Fig. S7). Under irradiation for 3 h, the H_2O_2 production over CN and CNT was already about to the peak and even showed a slight decrease. But its showed the sustained growth over ACNT, which indicated that the photo-generated H_2O_2 could be stable for a long time.

Photocatalytic production rate constants were calculated by using the integrated solution for a first-order kinetic reaction, $\ln(C_0/C) = kt$, (Fig. 5B) to compare the performance of the different catalysts. The H_2O_2 production rate constant for ACNT-5 was approximately 13 times higher than that of CN. The stability of ACNT-5 was tested over six experimental cycles (Fig. 5C). H_2O_2 production is maintained at 90 % after six cycles. The nanotube structure of ACNT-5 is maintained after six runs (Fig. 5D).

3.4. Photoelectric property

Several photoelectric properties of the catalysts were characterized to investigate the mechanism controlling the observed enhancements in photocatalytic activity (Fig. 6A and 6B). The dramatic reduction in PL emission intensity in sample ACNT-5, as compared to that of CN, suggests the effective separation of the photogenerated electron–hole pairs [42–44]. Small arcs in the Nyquist plots of ACNT-5 obtained via EIS reflect fast electron transfer and efficient charge separation [45,46]. The same findings can be obtained from the ns-level time-resolved fluorescence decay spectra shown in Fig. 6C and D. Changes in the tendency of decay time can be clearly observed in the fitted decay spectra. ACNT-5 exhibits a drastic decrease in fluorescence lifetime in comparison with that of CN. The reduction multipliers for ACNT-1, ACNT-5, and ACNT-10 are 5.3 times, 7.2 times, and 7.1 times, respectively (Fig. S8). These decreased lifetimes suggest the increased efficiency of charge separation and subsequent transfer of electrons and holes. Photogenerated carriers are then captured by reactive substrates at the surface leading to the observed reaction products [47,48]. The ability of the photocatalysts to absorb light and their band gaps were detected by UV-DRS (Fig. S9A). The ability of the photocatalysts to absorb light is improved in the ultraviolet region, which implies enhancements in photocatalytic activity [49,50]. The change in band structure may be an important factor for

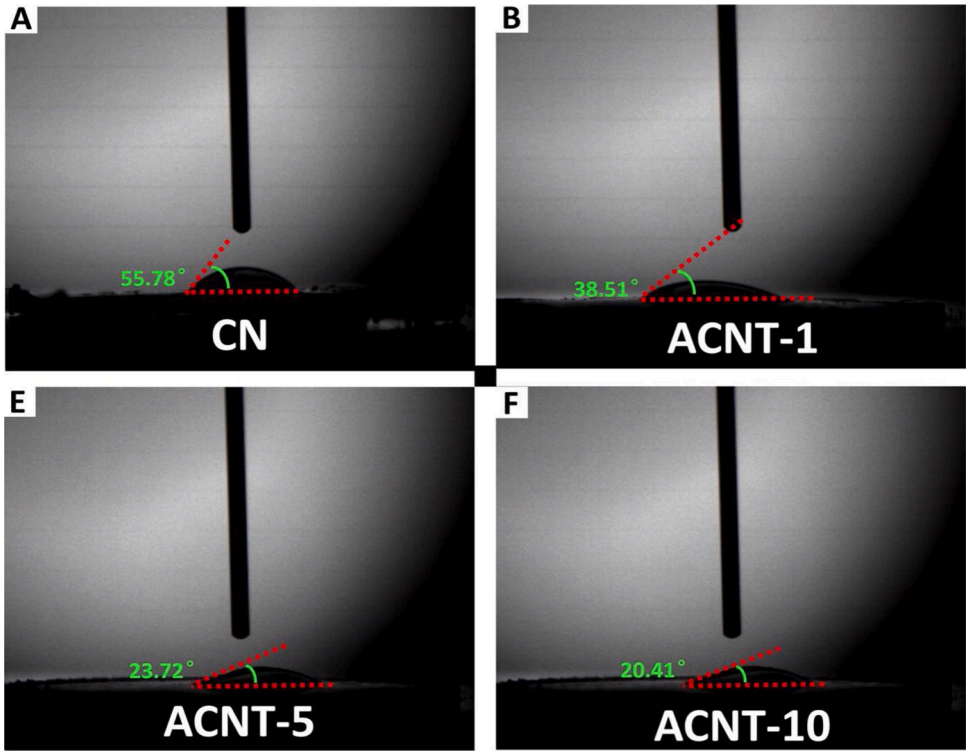

Fig. 4. (A–D) Contact angles of different catalysts.

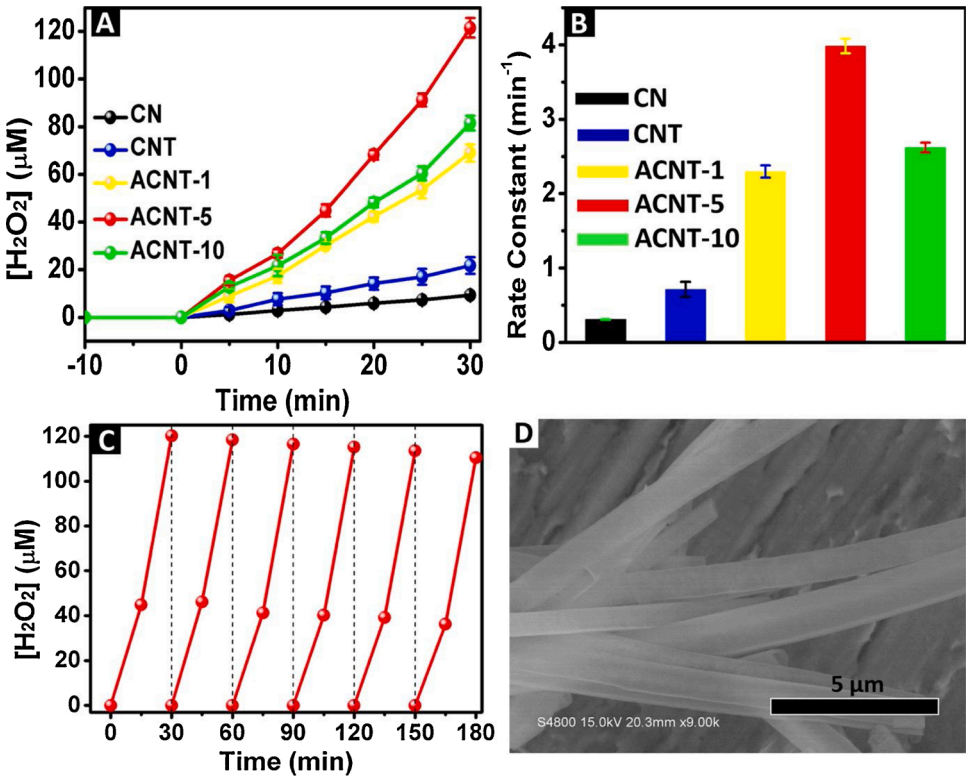

Fig. 5. (A) Comparison of photocatalytic H_2O_2 production over different catalysts. (B) Rate constant of the photocatalytic reaction with different catalysts. The error bars arise from the values extracted from several measurements on multiple catalysts. (C) Photocatalytic H_2O_2 production over ANCT-5 as a function of time. (D) FESEM image of ACNT-5 after six runs.

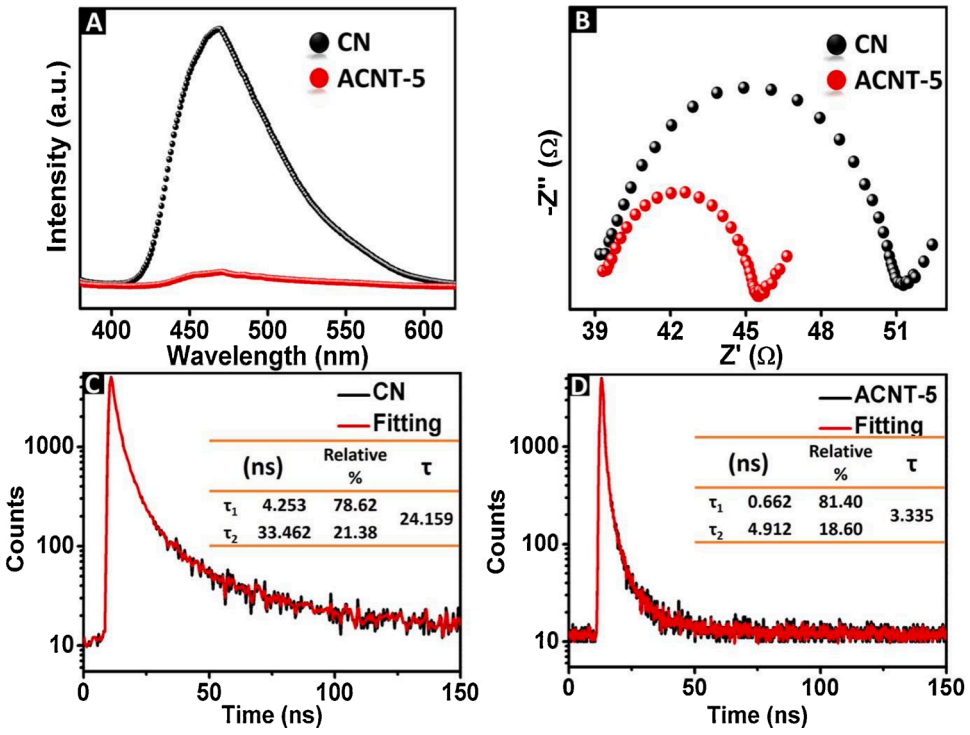

Fig. 6. (A) PL spectra of CN and ACNT-5. (B) EIS spectra of CN and ACNT-5. (C, D) Room-temperature ns-level time-resolved PL spectra of CN and ACNT-5 monitored under 469 nm excitation.

the improvement of photocatalytic activity. However, the band gap of the different catalysts in this study generally does not show remarkable changes (Fig. S9B).

3.5. The inhibitory effect of the in situ grafted hydroxyl groups on the decomposition of H_2O_2

The active species in the reactions were investigated by EPR and trapping experiments to explain the observed improvement in H_2O_2 production over ACNT compared with that over CN (Fig. 7). The sharp peak of $^{\bullet}O_2^-$ indicates that O_2 reduction to H_2O_2 ($2\,HO_2^{\bullet} \longrightarrow H_2O_2 + O_2$ or $O_2^- {}^{\bullet} + 2H^+ + \bar{e} \longrightarrow H_2O_2$) over CN is taking place. However, no $^{\bullet}O_2^-$ signal was not observed in the EPR spectrum of ACNT-5, the $^{\bullet}$OH signal was detected. However, ·OH is not the active species generating H_2O_2. Thus, three trapping experiments were performed to determine the appropriate mechanism; here, 0.005 mM of 1,4-benzoquinone (BQ, $^{\bullet}O_2^-$ scavenger), 0.01 mM of isopropanol (IPA, $^{\bullet}$OH scavenger), and 0.01 mM of triethanolamine (TEOA, h^+ scavenger) were separately added to the H_2O_2 production system. A decrease in H_2O_2 production of over 95 % was observed when BQ was added to the system with CN as the catalyst. This finding is completely consistent with the EPR results. In contrast, in the ACNT-5 system, BQ has little impact on H_2O_2 production, which suggests that $\cdot O_2^-$ is not primary factor for generating H_2O_2 over ACNT-5.

When IPA was added to the H_2O_2 production system, H_2O_2 in the ACNT-5 system decreased by 25 %. The separation efficiency of electron–hole pairs in the ACNT-5 system is maintained at high levels (see the PL, EIS, and ns-level time-resolved fluorescence decay spectra in Fig. 6), therefore, when OH is captured by IPA, the main reaction for H_2O_2 decomposition (Eq. (3), $H_2O_2 + H^+ + e^- \rightarrow H_2O + OH^{\bullet}$) is promoted, leading to a decrease in H_2O_2 production. In the h^+ trapping experiment, H_2O_2 production increases in the CN system due to the promotion of electron–hole pair separation, which is the main limitation of the CN system. The OH— bond cannot be oxidized to $OH^{\bullet}$ in the ACNT-5 system because of h^+ capture, consequently H_2O_2 decomposition is minimal. More importantly, surface > OH groups serve as electron traps forming surface bound ·OH thus limiting H_2O_2 decomposition ($2 > OH\cdot \rightarrow H_2O_2$). The H_2O_2 decomposition experiment was carried out to verify this mechanism. As shown in Fig. S10, almost all the H_2O_2 were decomposed for CN and more than 65 % of H_2O_2 were maintained for ACNT-5 after 1 h. At the beginning, a great quantity of H_2O_2(1 mM) inhibited the production reaction, the photo-generated electrons were mainly involved in the decomposition of H_2O_2 for CN. And for ACNT-5, surface > OH groups were reacted with h^+, the resulant $OH^{\bullet}$ inhibited Eq. (3) and a large amount of H_2O_2 was retained.

These results show that ACNT has excellent photoelectric properties that enable efficient electron–hole separation and surface trapping of both electrons and holes.

3.6. The capture of h^+ and the generation of H^+ by the in situ grafted hydroxyl groups

The role of protons (i.e., $O_2 + 2H^+ + 2e^- \rightarrow H_2O_2$) in the overall reaction was investigated. H_2O_2 production depends on pH since the reaction is governed by proton-coupled electron transfer favored by low pH [20,51]. Therefore, the pH was monitored during course of H_2O_2 production as shown in Fig. 8. In the CN system, the pH rose slightly during dark adsorption with and without EtOH due to the protonation of amino groups on the CN surface (Eq. (8)). The pH decreased as the reaction proceeds after introduction of light, with H^+ generated from the oxidation of H_2O by photogenerated holes. When a sacrificial agent or hole trap (EtOH) is used, the photogenerated holes are used to oxidize the electron donating substrate (e.g., $R\text{-}CH_2OH + 2h^+ \rightarrow R\text{-}CHO + 2H^+$). Furthermore, H^+ production during water oxidation results in reduction in pH. Consequently, the amount of H_2O_2 was three time the obtained in the spontaneous CN system (Fig. 8A). Fig. 8B reveals the role of the sacrificial electron donor in the spontaneous CN system. However, in the ACNT-5 system, catalyst has intrinsically a source of electron donor sites. Although the original pH of the spontaneous ACNT-5 system was substantially higher than that of the spontaneous CN system (Fig. 8C), the pH began to decrease during dark adsorption in ACNT-5 system.

$$R - NH_2 + H_2O \rightarrow R - NH_3^+ + OH^- \quad (8)$$

$$RCH_2OH + 2h^+ \rightarrow RCHO + 2H^+ \quad (9)$$

$$RCHO + 2h^+ \rightarrow RC \equiv O^+ + H^+ \quad (10)$$

$$RC \equiv O^+ + H_2O \rightarrow RCOOH + H^+ \quad (11)$$

$$CH_3COOH \rightleftharpoons CH_3CO_2^- + H^+ \quad (12)$$

When the light was switched on, *in situ* grafted surface > OH groups served as hole traps to produce H^+ as shown in Eqs. (9)–(12). The pH

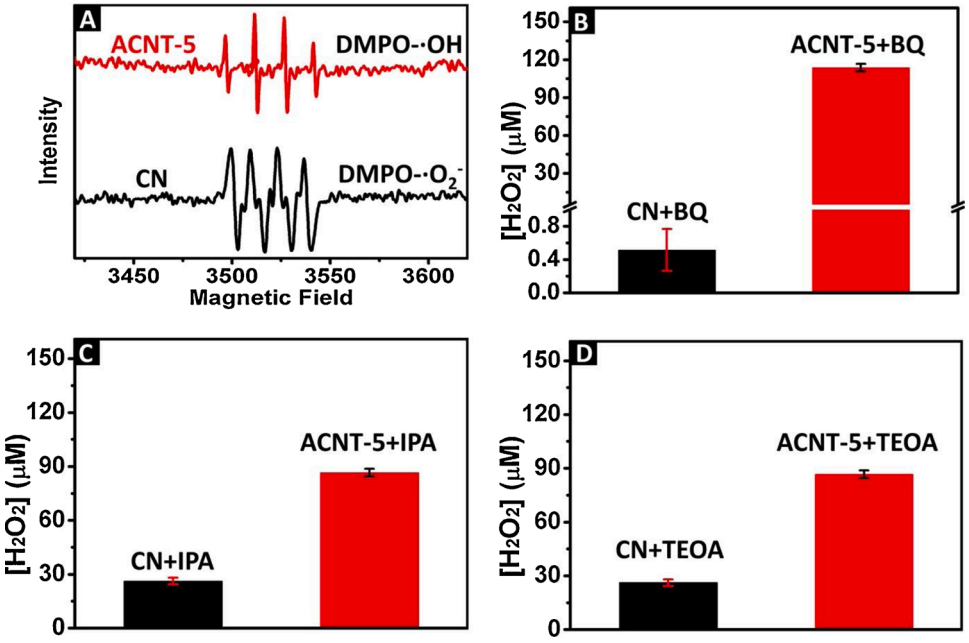

Fig. 7. (A) Comparison of EPR peaks during H_2O_2 production in the CN and ACNT-5 systems. H_2O_2 production with (B) BQ, (C) IPA, and (D) TEOA over CN and ACNT. The error bars arise from values extracted from several measurements on multiple catalysts.

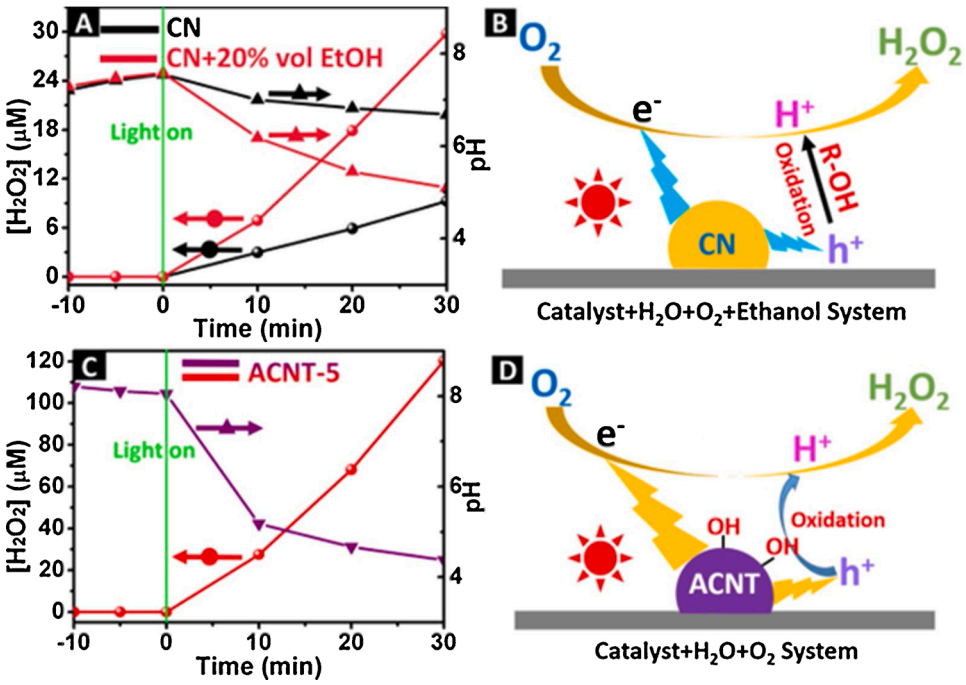

Fig. 8. (A) Photocatalytic H_2O_2 production by CN with and without sacrificial agent and the pH of both systems. (B) Schematic of photocatalytic H_2O_2 production in the CN system with a sacrificial agent. (C) Photocatalytic H_2O_2 production in the spontaneous ACNT-5 system. (D) Schematic of photocatalytic H_2O_2 production in the spontaneous ACNT-5 system.

was quickly reduced and reached 4.38 in the spontaneous ACNT-5 system; this pH is even lower than that of the CN system with a sacrificial agent (pH = 5.10) due to lower hydroxyl radical production. Acetic acid deportation results in greater H^+ production and thus a lower pH in the ACNT-5 system. Fig. 8D shows the route through which key components (e^- and H^+) of the ACNT-5 system are generated. The ACNT catalyst improved photocatalytic activity when compared to most of the spontaneous systems listed in Table S1.

3.7. *The stability of the in situ grafted hydroxyl groups*

The stability of the *in situ* grafted OH groups was examined and any quantitative changes in the surface groups were determined (Fig. S11). First, the peak of the *in situ* grafted OH groups (at 2140 cm^{-1}) did not decrease significantly. Second, the ratio of I_1/I_2 of ACNT-5 increased after six runs because of the partial dissociation of water molecules adsorbed on the CN surface. The adsorption rate was lower than the surface dissociation rate, and this difference led to increases in I_1/I_2. Therefore, these results when combined with the result of repeated experiments as shown in Fig. 5C, we conclude the ACNT photocatalytic system in oxygenated water is reasonably stable for the photocatalytic H_2O_2 production.

4. Conclusions

In summary, an ACNT photocatalyst with *in situ* grafted OH groups were successfully prepared via an optimized hydrothermal-cum-calcination method. The catalyst exhibited excellent photoelectric properties resulting from the synergistic effects of its nanotube structure and grafted OH groups. Self-decomposition of H_2O_2 was effectively prevented by the OH groups of the photocatalyst, with excellent H_2O_2 production achieved in a spontaneous system without sacrificial agents. This work provides a new strategy for developing efficient, metal-free photocatalysts for H_2O_2 production in illuminated systems.

CRediT authorship contribution statement

Liang Zhou: Conceptualization, Investigation, Writing - original draft. **Juying Lei:** Data curation, Supervision. **Fuchen Wang:** Resources. **Lingzhi Wang:** Resources, Methodology. **Michael R. Hoffmann:** Writing - review & editing. **Yongdi Liu:** Writing - review & editing, Funding acquisition. **Su-Il In:** Writing - review & editing. **Jinlong Zhang:** Project administration.

Declaration of Competing Interest

The authors declare that they have no known competing financial interests or personal relationships that could have appeared to influence the work reported in this paper.

Acknowledgments

The authors gratefully acknowledge the National Key Research and Development Program (2016YFA0204200), the support of the National Natural Science Foundation of China (22006038, 21777044 and 22076046), the China Postdoctoral Science Foundation (2020M681209), the Science and Technology Commission of Shanghai Municipality (19ZR1472400, 19230711300). This research was also supported by Korean National Research Foundation (2017R1E1A1A01074890).

Appendix A. Supplementary data

Supplementary material related to this article can be found, in the online version, at doi:https://doi.org/10.1016/j.apcatb.2021.119993.

References

[1] J.O. Thostenson, E. Ngaboyamahina, K.L. Sellgren, B.T. Hawkins, J.R. Piascik, E.J. D. Klem, C.B. Parker, M.A. Deshusses, B.R. Stoner, J.T. Glass, Enhanced H_2O_2 production at reductive potentials from oxidized boron-doped ultrananocrystalline diamond electrodes, ACS Appl. Mater. Interfaces 9 (2017) 16610–16619.

[2] Y. Yang, Z. Zeng, G. Zeng, D. Huang, R. Xiao, C. Zhang, C. Zhou, W. Xiong, W. Wang, M. Cheng, W. Xue, H. Guo, X. Tang, D. He, Ti_3C_2 Mxene/porous g-C_3N_4 interfacial schottky junction for boosting spatial charge separation in photocatalytic H_2O_2 production, Appl. Catal. B-Environ. 258 (2019), 117956.

[3] Y.-H. Wang, M.L. Pegis, J.M. Mayer, S.S. Stahl, Molecular cobalt catalysts for O_2 reduction: low-overpotential production of H_2O_2 and comparison with iron-based catalysts, J. Am. Chem. Soc. 139 (2017) 16458–16461.

[4] S. Wu, H. Yu, S. Chen, X. Quan, Enhanced photocatalytic H_2O_2 production over carbon nitride by doping and defect engineering, ACS Catal. 10 (2020) 14380–14389.

[5] J. Lei, B. Chen, W. Lv, L. Zhou, L. Wang, Y. Liu, J. Zhang, Robust photocatalytic H_2O_2 production over inverse opal g-C_3N_4 with carbon vacancy under visible light, ACS Sustain. Chem. Eng. 7 (2020) 16467–16473.

[6] P. Zhang, Y. Tong, Y. Liu, J.J.M. Vequizo, H. Sun, C. Yang, A. Yamakata, F. Fan, W. Lin, X. Wang, W. Choi, Heteroatom dopants promote two-electron O_2 reduction for photocatalytic production of H_2O_2 on polymeric carbon nitride, Angew. Chem. Int. Ed. 59 (2020) 16209–16217.

[7] Z. Jiang, L. Wang, J. Lei, Y. Liu, J. Zhang, Photo-fenton degradation of phenol by CdS/rGO/Fe^{2+} at natural pH with in situ-generated H_2O_2, Appl. Catal. B-Environ. 241 (2019) 367–374.

[8] Y. Peng, L. Wang, Y. Liu, H. Chen, J. Lei, J. Zhang, Visible-light-driven photocatalytic H_2O_2 production on g-C_3N_4 loaded with CoP as a noble metal free cocatalyst, Eur. J. Inorg. Chem. 2017 (2017) 4797–4802.

[9] Y. Zhao, Y. Liu, J. Cao, H. Wang, M. Shao, H. Huang, Y. Liu, Z. Kang, Efficient production of H_2O_2 via two-channel pathway over ZIF-8/C_3N_4 composite photocatalyst without any sacrificial sgent, Appl. Catal. B-Environ. 278 (2020), 119289.

[10] Z. Teng, W. Cai, W. Sim, Q. Zhang, C. Wang, C. Su, T. Ohno, Photoexcited single metal atom catalysts for heterogeneous photocatalytic H_2O_2 production: pragmatic guidelines for predicting charge separation, Appl. Catal. B-Environ. 282 (2021), 119589.

[11] Y. Wanga, D. Menga, X. Zhao, Visible-light-driven H_2O_2 production from O_2 reduction with nitrogen vacancy-rich and porous graphitic carbon nitride, Appl. Catal. B-Environ. 273 (2020), 119064.

[12] C. Krishnaraj, H.S. Jena, L. Bourda, A. Laemont, P. Pachfule, J. Roeser, C. V. Chandran, S. Borgmans, S.M.J. Rogge, K. Leus, C.V. Stevens, J.A. Martens, V. V. Speybroeck, E. Breynaert, A. Thomas, P.V. Voort, Strongly reducing (diarylamino)benzene-based covalent organic framework for metal-free visible light photocatalytic H_2O_2 generation, J. Am. Chem. Soc. 142 (2020) 20107–20116.

[13] J. Zhang, L. Zheng, F. Wang, C. Chen, H. Wu, S.A.K. Leghari, M. Long, The Critical role of furfural alcohol in photocatalytic H_2O_2 production on TiO_2, Appl. Catal. B-Environ. 269 (2020), 118770.

[14] M. Teranishi, S.-i. Naya, H. Tada, In situ liquid phase synthesis of hydrogen peroxide from molecular oxygen using gold nanoparticle-loaded titanium (IV) dioxide photocatalyst, J. Am. Chem. Soc. 132 (2010) 7850–7851.

[15] H.-i. Kim, O.S. Kwon, S. Kim, W. Choi, J.-H. Kim, Harnessing low energy photons (635 nm) for the production of H_2O_2 using upconversion nanohybrid photocatalysts, Energy Environ. Sci. 9 (2016) 1063–1073.

[16] Y. Shiraishi, Y. Kofuji, H. Sakamoto, S. Tanaka, S. Ichikawa, T. Hirai, Effects of surface defects on photocatalytic H_2O_2 production by mesoporous graphitic carbon nitride under visible light irradiation, ACS Catal. 5 (2015) 3058–3066.

[17] Y. Shiraishi, S. Kanazawa, Y. Kofuji, H. Sakamoto, S. Ichikawa, S. Tanaka, T. Hirai, Sunlight-driven hydrogen peroxide production from water and molecular oxygen by metal-free photocatalysts, Angew. Chem. Int. Ed. 53 (2014) 13454–13459.

[18] Y. Kofuji, Y. Isobe, Y. Shiraishi, H. Sakamoto, S. Tanaka, S. Ichikawa, T. Hirai, Carbon nitride–aromatic diimide–graphene nanohybrids: metal-free photocatalysts for solar-to-hydrogen peroxide energy conversion with 0.2% efficiency, J. Am. Chem. Soc. 138 (2016) 10019–10025.

[19] H. Hirakawa, S. Shiota, Y. Shiraishi, H. Sakamoto, S. Ichikawa, T. Hirai, Au nanoparticles supported on $BiVO_4$: effective inorganic photocatalysts for H_2O_2 production from water and O_2 under visible light, ACS Catal. 6 (2016) 4976–4982.

[20] G.-h. Moon, W. Kim, A.D. Bokare, N.-e. Sung, W. Choi, Solar production of H_2O_2 on reduced graphene oxide–TiO_2 hybrid photocatalysts consisting of earth-abundant elements only, Energy Environ. Sci. 7 (2014) 4023–4028.

[21] D. Tsukamoto, A. Shiro, Y. Shiraishi, Y. Sugano, S. Ichikawa, S. Tanaka, T. Hirai, Photocatalytic H2O2 production from ethanol/O2 system using TiO2 loaded with Au–Ag bimetallic alloy nanoparticles, ACS Catal. 2 (2012) 599–603.

[22] H. Kim, J. Lim, S. Lee, H.-H. Kim, C. Lee, J. Lee, W. Choi, Spontaneous generation of H_2O_2 and hydroxyl radical through O_2 reduction on copper phosphide under ambient aqueous condition, Environ. Sci. Technol. 53 (2019) 2918–2925.

[23] K. Fuku, R. Takioka, K. Iwamura, M. Todoroki, K. Sayama, N. Ikenaga, Photocatalytic H_2O_2 production from O_2 under visible light irradiation over phosphate ion-coated Pd nanoparticles-supported $BiVO_4$, Appl. Catal. B-Environ. 272 (2020), 119003.

[24] L. Zhou, J. Feng, B. Qiu, Y. Zhou, J. Lei, M. Xing, L. Wang, Y. Zhou, Y. Liu, J. Zhang, Ultrathin g-C_3N_4 nanosheet with hierarchical pores and desirable energy band for highly efficient H_2O_2 production, Appl. Catal. B-Environ. 267 (2020), 118396.

[25] S. Guo, Y. Tang, Y. Xie, C. Tian, Q. Feng, W. Zhou, B. Jiang, P-doped tubular g-C_3N_4 with surface carbon defects: universal synthesis and enhanced visible-light photocatalytic hydrogen production, Appl. Catal. B-Environ. 218 (2017) 664–671.

[26] Y.-S. Jun, E.Z. Lee, X. Wang, W.H. Hong, G.D. Stucky, A. Thomas, From melamine-cyanuric acid supramolecular aggregates to carbon nitride hollow spheres, Adv. Funct. Mater. 23 (2013) 3661–3667.

[27] T. Sano, S. Tsutsui, K. Koike, T. Hirakawa, Y. Teramoto, N. Negishi, K. Takeuchi, Activation of graphitic carbon nitride (g-C_3N_4) by alkaline hydrothermal treatment for photocatalytic NO oxidation in gas phase, J. Mater. Chem. A 1 (2013) 6489–6496.

[28] X. Sun, D. Jiang, L. Zhang, W. Wang, Alkaline modified g-C_3N_4 photocatalyst for high selective oxide coupling of benzyl alcohol to benzoin, Appl. Catal. B-Environ. 220 (2018) 553–560.

[29] G. Xu, H. Zhang, J. Wei, H.-X. Zhang, X. Wu, Y. Li, C. Li, J. Zhang, J. Ye, Integrating the g-C_3N_4 nanosheet with B–H bonding decorated metal–organic framework for CO_2 activation and photoreduction, ACS Nano 12 (2018) 5333–5340.

[30] Z. Pan, G. Zhang, X. Wang, Polymeric carbon nitride/reduced graphene oxide/Fe_2O_3: all-solid-state Z-Scheme system for photocatalytic overall water splitting, Angew. Chem. Int. Ed. 131 (2019) 7176–7180.

[31] L. Zhou, Y. Tian, J. Lei, L. Wang, Y. Liu, J. Zhang, Self-modification of g-C_3N_4 with its quantum dots for enhanced photocatalytic activity, Catal. Sci. Technol. 8 (2018) 2617–2623.

[32] A.A. Khan, M. Tahir, A. Bafaqeer, Constructing a stable 2D layered Ti_3C_2 MXene cocatalyst-assisted TiO_2/g-C_3N_4/Ti_3C_2 heterojunction for tailoring photocatalytic bireforming of methane under visible light, Energy Fuels 34 (2020) 9810–9828.

[33] J. Li, Y. Yin, E. Liu, Y. Ma, J. Wan, J. Fan, X. Hu, In situ growing Bi_2MoO_6 on g-C_3N_4 nanosheets with enhanced photocatalytic hydrogen evolution and disinfection of bacteria under visible light irradiation, J. Hazard. Mater. 321 (2017) 183–192.

[34] X. Cai, J. He, L. Chen, K. Chen, Y. Li, K. Zhang, Z. Jin, J. Liu, C. Wang, X. Wang, L. Kong, J. Liu, A 2D-g-C_3N_4 nanosheet as an eco-friendly adsorbent for various environmental pollutants in water, Chemosphere 171 (2017) 192–201.

[35] Y. Li, H. Xu, S. Ouyang, D. Lu, X. Wang, D. Wang, J. Ye, In situ surface alkalinized g-C_3N_4 toward enhancement of photocatalytic H_2 evolution under visible-light irradiation, J. Mater. Chem. A 4 (2016) 2943–2950.

[36] Y. Li, S. Ouyang, H. Xu, X. Wang, Y. Bi, Y. Zhang, J. Ye, Constructing solid–Gas-Interfacial Fenton reaction over Alkalinized-C_3N_4 photocatalyst to achieve apparent quantum yield of 49% at 420 nm, J. Am. Chem. Soc. 138 (2016) 13289–13297.

[37] Q. Dong, Y. Chen, L. Wang, S. Ai, H. Ding, Cu-modified alkalinized g-C_3N_4 as photocatalytically assisted heterogeneous Fenton-like catalyst, Appl. Surf. Sci. 426 (2017) 1133–1140.

[38] G. Fan, R. Ning, Z. Yan, J. Luo, B. Du, J. Zhan, L. Liu, J. Zhang, Double photoelectron-transfer mechanism in Ag−AgCl/WO_3/g-C_3N_4 photocatalyst with enhanced visible-light photocatalytic activity for trimethoprim degradation, J. Hazard. Mater. 403 (2021), 123964.

[39] M. Wu, J.-M. Yan, X.-n. Tang, M. Zhao, Q. Jiang, Synthesis of potassium-modified graphitic carbon nitride with high photocatalytic activity for hydrogen evolution, ChemSusChem 7 (2014) 2654–2658.

[40] S. Song, C. Lu, X. Wu, S. Jiang, C. Sun, Z. Le, Strong base g-C_3N_4 with perfect structure for photocatalytically eliminating formaldehyde under visible-light irradiation, Appl. Catal. B-Environ. 227 (2018) 145–152.

[41] D. Qi, M. Xing, J. Zhang, Hydrophobic Carbon-doped TiO_2/MCF-F composite as a high performance photocatalyst, J. Phys. Chem. C 118 (2014) 7329–7336.

[42] S. Wu, X. Tan, J. Lei, H. Chen, L. Wang, J. Zhang, Ga-doped and Pt-loaded porous TiO_2–SiO_2 for photocatalytic nonoxidative coupling of methane, J. Am. Chem. Soc. 141 (2019) 6592–6600.

[43] L. Zhou, L. Wang, J. Lei, Y. Liu, J. Zhang, Fabrication of TiO_2/Co-g-C_3N_4 heterojunction catalyst and its photocatalytic performance, Catal. Commun. 89 (2017) 125–128.

[44] X. Xiao, Y. Gao, L. Zhang, J. Zhang, Q. Zhang, Q. Li, H. Bao, J. Zhou, S. Miao, N. Chen, J. Wang, B. Jiang, C. Tian, H. Fu, A promoted charge separation/transfer system from Cu single atoms and C_3N_4 layers for efficient photocatalysis, Adv. Mater. 32 (2020), 2003082.

[45] B. Qiu, Q. Zhu, M. Du, L. Fan, M. Xing, J. Zhang, Efficient solar light harvesting CdS/Co_9S_8 hollow cubes for Z-Scheme photocatalytic water splitting, Angew. Chem. Int. Ed. 56 (2017) 2684–2688.

[46] F. Liu, J. Yu, G. Tu, L. Qu, J. Xiao, Y. Liu, L. Wang, J. Lei, J. Zhang, Carbon nitride coupled Ti-SBA15 catalyst for visible-light-driven photocatalytic reduction of Cr (VI) and the synergistic oxidation of phenol, Appl. Catal. B-Environ. 201 (2017) 1–11.

[47] A. Kongkanand, K. Tvrdy, K. Takechi, M. Kuno, P.V. Kamat, Quantum dot solar cells. Tuning photoresponse through size and shape control of CdSe−TiO_2 architecture, J. Am. Chem. Soc. 130 (2008) 4007–4015.

[48] T.-T. Yang, W.-T. Chen, Y.-J. Hsu, K.-H. Wei, T.-Y. Lin, T.-W. Lin, Interfacial charge carrier dynamics in Core−Shell Au-CdS nanocrystals, J. Phys. Chem. C 114 (2010) 11414–11420.

[49] Y. Cao, Z. Xing, Z. Li, X. Wu, M. Hu, X. Yan, Q. Zhu, S. Yang, W. Zhou, Mesoporous black TiO_{2-x}/Ag nanospheres coupled with g-C_3N_4 nanosheets as 3D/2D ternary heterojunctions visible light photocatalysts, J. Hazard. Mater. 343 (2018) 181–190.

[50] G. Zhang, G. Li, T. Heil, S. Zafeiratos, F. Lai, A. Savateev, M. Antonietti, X. Wang, Tailoring the grain boundary chemistry of polymeric carbon nitride for enhanced solar hydrogen production and CO_2 reduction, Angew. Chem. Int. Ed. 58 (2019) 3433–3437.

[51] Z. Qiang, J.-H. Chang, C.-P. Huang, Electrochemical generation of hydrogen peroxide from dissolved oxygen in acidic solutions, Water Res. 36 (2002) 85–94.